

Supporting Information

Ni non-equivalent doped La-MOF toward enhanced photocatalytic CO₂ reduction through oxygen vacancy regulation and electronic structure optimization

Tongzheng Zhang^a, Zhaohui Huang^a, Guanshun Xie^a, Le Liao^a, Changqiang Yu^a, Xiuqiang Xie^{*a}, and Nan Zhang^{*a}

^a College of Materials Science and Engineering, Hunan University, P. R. China

1. Experimental details

1.1 Materials characterization: Crystal forms of catalysts were analyzed by X-ray diffraction (XRD) on a Bruker D8 Advance X-ray diffractometer using Cu-K α radiation. High resolution transmission electron microscopy (HR-TEM, JEM-2100 F), elemental mapping using energy-dispersive X-ray spectroscopy (EDX), and field emission scanning electron microscopy (FE-SEM, Hitachi Regulus 8100) were employed to determine the structure and elemental distribution of the catalysts. X-ray photoelectron spectroscopy (XPS) was performed on an Esca lab 250Xi spectrometer, and the binding energies were referenced to the C 1s peak at 284.8 eV. N₂ adsorption/desorption isotherms and CO₂ adsorption isotherms were recorded and analyzed using a Micromeritics ASAP 2020 system. Catalysts were degassed in vacuum at 120 °C for 6 h prior to measurement. Fourier transform infrared spectroscopy (FTIR) and Raman spectroscopy were conducted on a Nexus 670 FTIR spectrometer and a DXR 2xi Raman spectrometer, respectively. The diffuse reflectance spectra (DRS) of the samples were acquired using a UV-vis spectrophotometer (Shimadzu, UV-2550, Japan). The energy band structure of the samples was determined by measuring ultraviolet photoelectron spectra (UPS, ESCALAB 250Xi, Thermo Fisher Scientific, USA). Time-resolved photoluminescence (PL) spectra and

steady-state PL spectra of the photocatalytic reaction systems were recorded and analyzed on an FLS980 spectrometer (540 nm, room temperature). (Shimadzu, Japan). Electron spin resonance (ESR) was performed on an ESR spectrometer (MEX-nano, Bruker, DEU). In situ diffuse reflectance infrared Fourier transform spectroscopy (DRIFTS) was obtained on a Nicolet iS50 FTIR spectrometer (Thermo Fisher, USA) equipped with a mercury cadmium telluride detector. In situ irradiated X-ray photoelectron spectroscopy (ISI-XPS) was conducted on a Thermo Fisher Escalab 250xi with an Al K α radiation hemispherical electron energy analyzer and a 300 W Xe arc lamp (PLS-SXE300D, Beijing Perfect Light Co., Ltd) with a 420 nm cut-off filter being placed. In the process of ISI-XPS characterization, the binding energy changes of the sample under visible-near infrared light irradiation of 20 cm ($\lambda > 420$ nm), darkness in a vacuum atmosphere, and after five minutes of illumination were studied. All binding energies were calibrated with the C 1s peak at 284.8 eV. To prepare the sample: accurately weigh 20 mg of the catalyst and 2 mg of [Ru(bpy)₃]Cl₂. The components were dispersed in deionized water and ultrasonically dispersed for 5 minutes to ensure that the dispersion was completely uniform to obtain La/Ni-MOF-3 adsorbed [Ru(bpy)₃]Cl₂.¹

1.2 Photoelectrochemical measurements: Photoelectrochemical properties were assessed on a CHI 660E electrochemical station (Shanghai Chenhua, China) in a three-electrode quartz cell containing 40 mL of electrolyte, with Pt plate (10 mm \times 10 mm) and Ag/AgCl employed as the counter electrode and reference electrode, respectively. For preparing working electrodes, fluorine-doped tin oxide (FTO) glass was ultrasonic washed with ethanol for 30 min and dried at 333 K, onto which scotch tape with the 0.25 cm² round-shaped hole was stuck. 5 mg of the samples was dispersed in 0.5 mL of N,N-dimethylformamide (DMF) assisted by ultrasonic concussion to form quasi steady suspension, which was then spread onto the hole left on the pretreated FTO glass. After drying naturally in the air, the scotch tape was unstuck, and the uncoated section of the electrode was segregated with epoxy resin. A 300 W Xe lamp system (PLS SXE300+, Beijing Perfect Light Co., Ltd.) equipped with a 420 nm cut-off filter was used as the irradiation source. The electrochemical impedance spectroscopy (EIS) experiments were conducted with the electrolyte of 0.5 M KCl aqueous solution containing 0.01 M

$\text{K}_3[\text{Fe}(\text{CN})_6]/\text{K}_4[\text{Fe}(\text{CN})_6]$ (1:1) under open-circuit potential conditions. The cathodic polarization curves were obtained using the linear sweep voltammetry (LSV) technique with a scan rate of 0.05 mV s^{-1} in 0.1 M NaHCO_3 aqueous solution under continuous bubbling of CO_2 or Ar. The Mott-Schottky (M-S) experiments were obtained in $0.2 \text{ M Na}_2\text{SO}_4$ aqueous solution.

2. Figures and tables

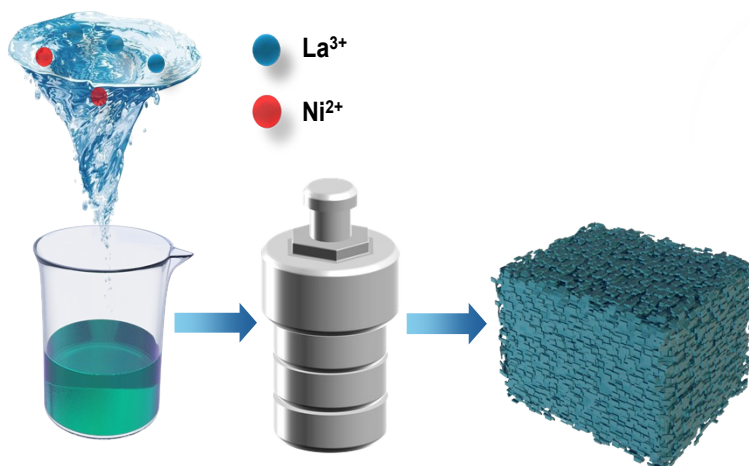


Figure S1. Synthesis diagram of bimetallic MOFs.

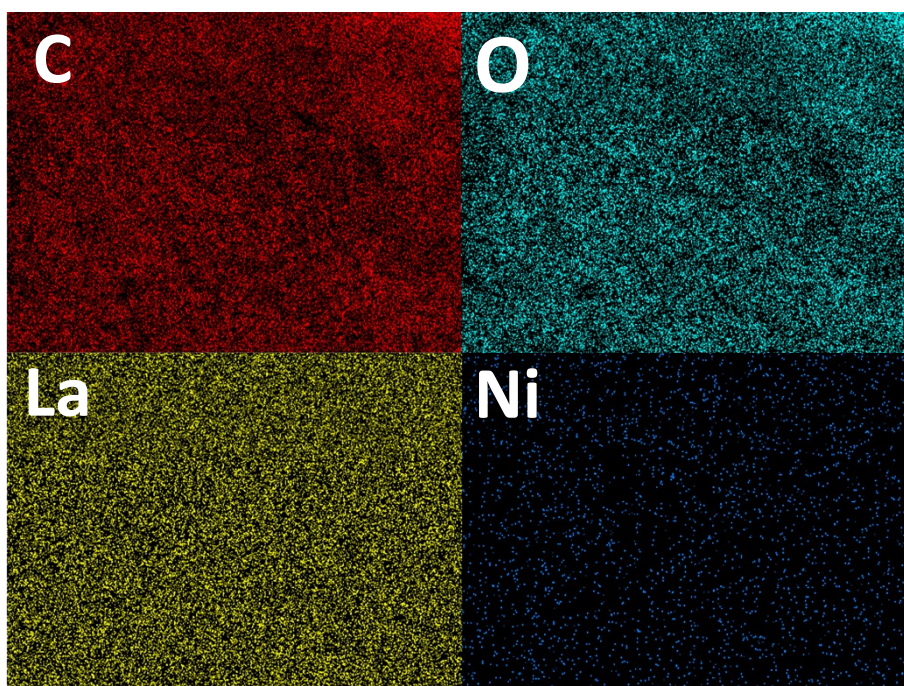


Figure S2. Elemental mapping images of the La/Ni-MOF-3 sample.

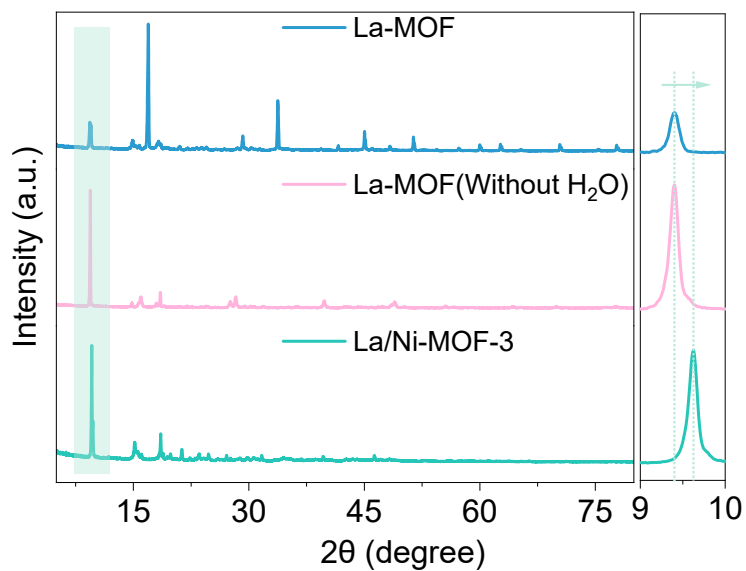


Figure S3. The XRD patterns of La/Ni-MOF-3 and La-MOF samples prepared by different reaction solvent compositions (more specifically, La-MOF is prepared in the solvent of DMF, H₂O and CH₃CH₂OH as described in the experimental section; La-MOF (Without H₂O) is prepared by adjusting the solvent as indicated in the bracket).

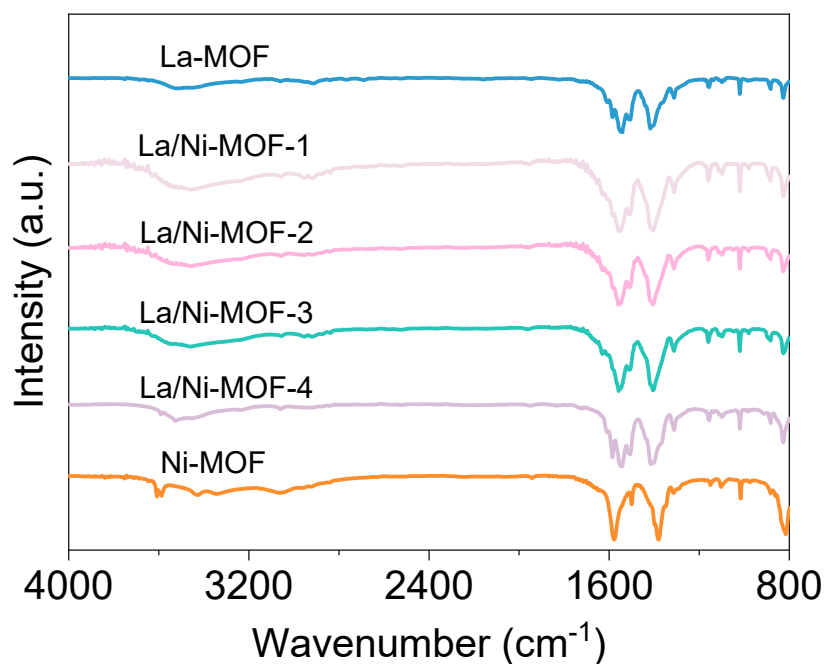


Figure S4. FTIR spectra of La-MOF, Ni-MOF, and La/Ni-MOF-*X* (*X* = 1, 2, 3, and 4).

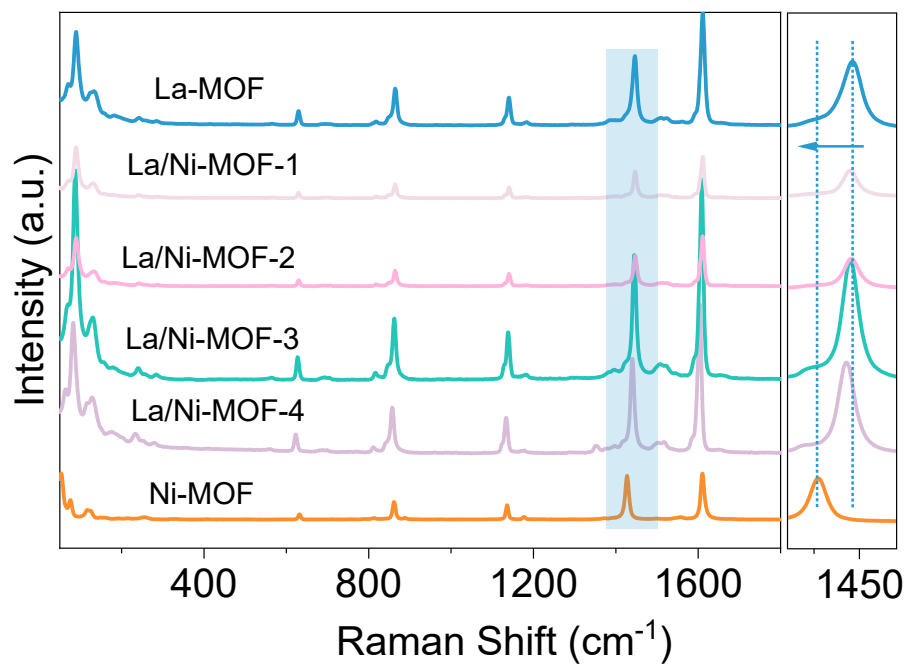


Figure S5. Raman spectra of La-MOF, Ni-MOF, and La/Ni-MOF- X ($X = 1, 2, 3,$ and 4).

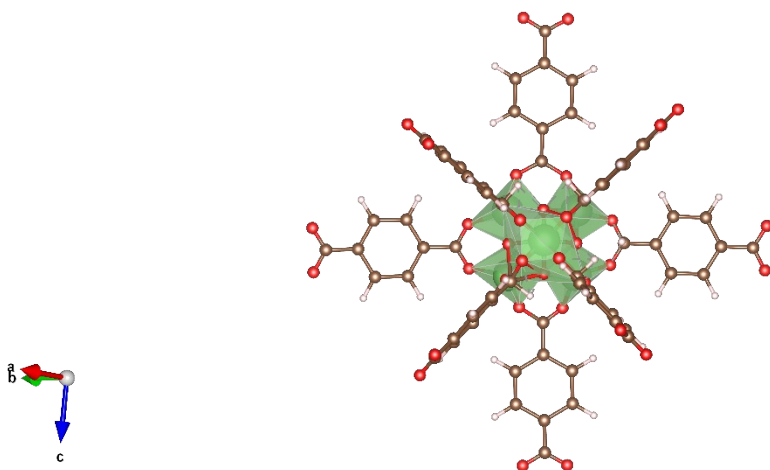


Figure S6. La-MOF crystal structure diagram.

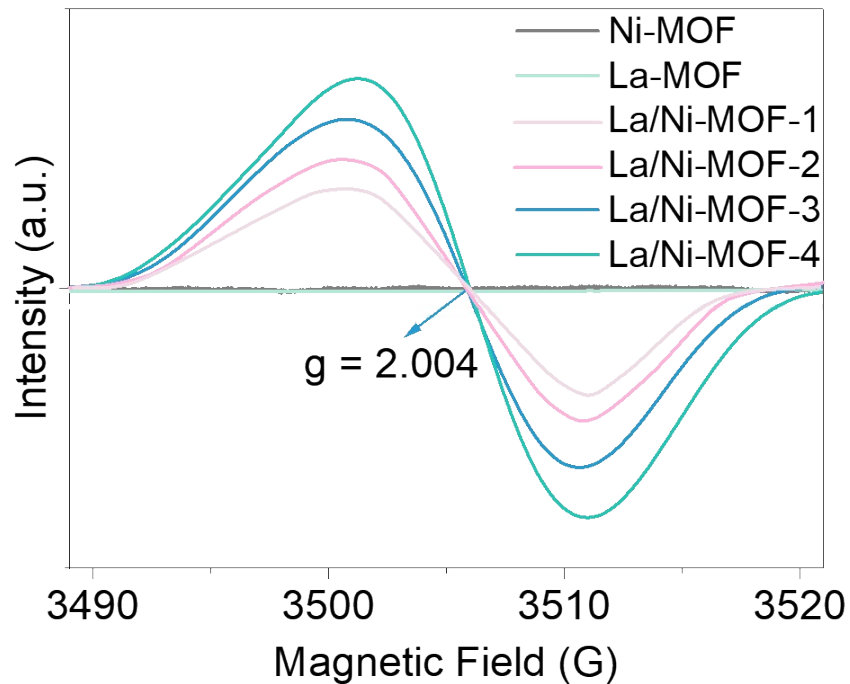


Figure S7. EPR spectra of La-MOF, Ni-MOF, and La/Ni-MOF- X ($X = 1, 2, 3,$ and 4).

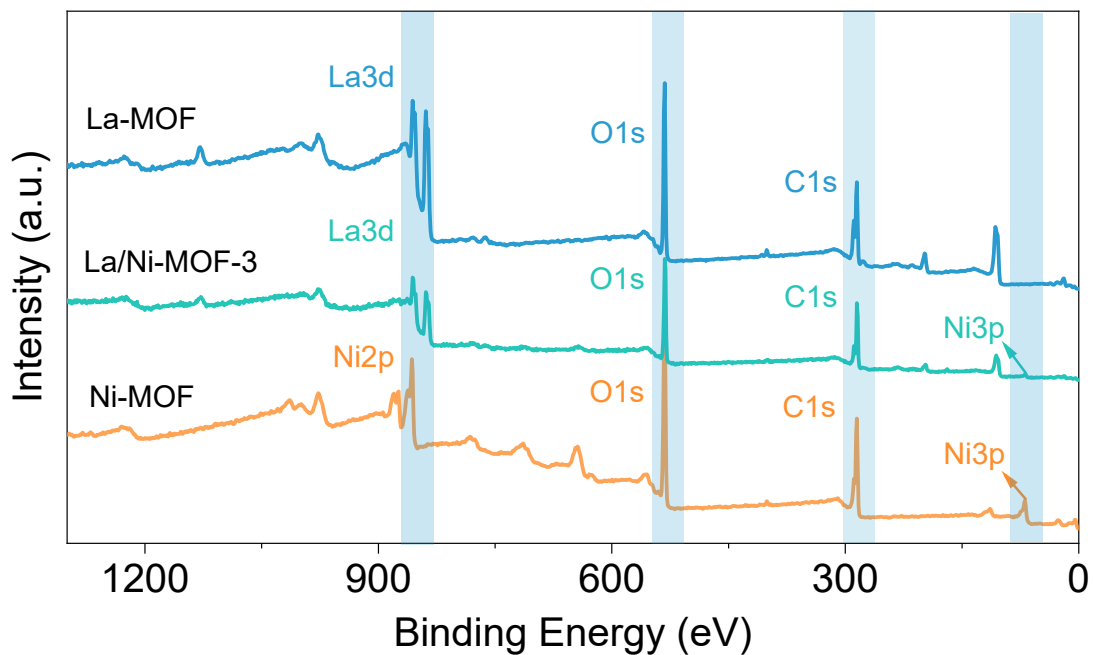


Figure S8. The XPS spectra of the as-prepared La-MOF, Ni-MOF, and La/Ni-MOF-3 samples.

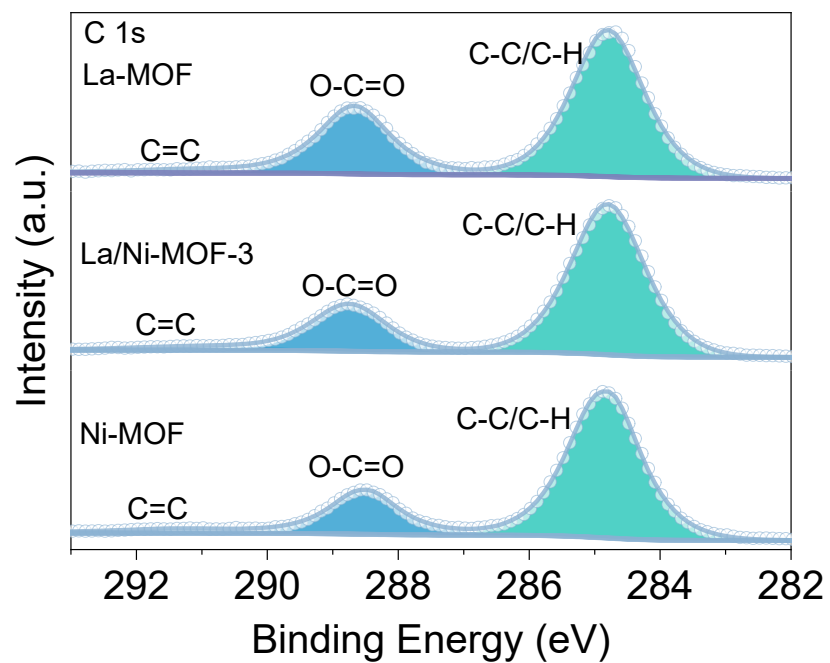


Figure S9. High-resolution C 1s XPS spectra of La-MOF, Ni-MOF, and La/Ni-MOF-3.

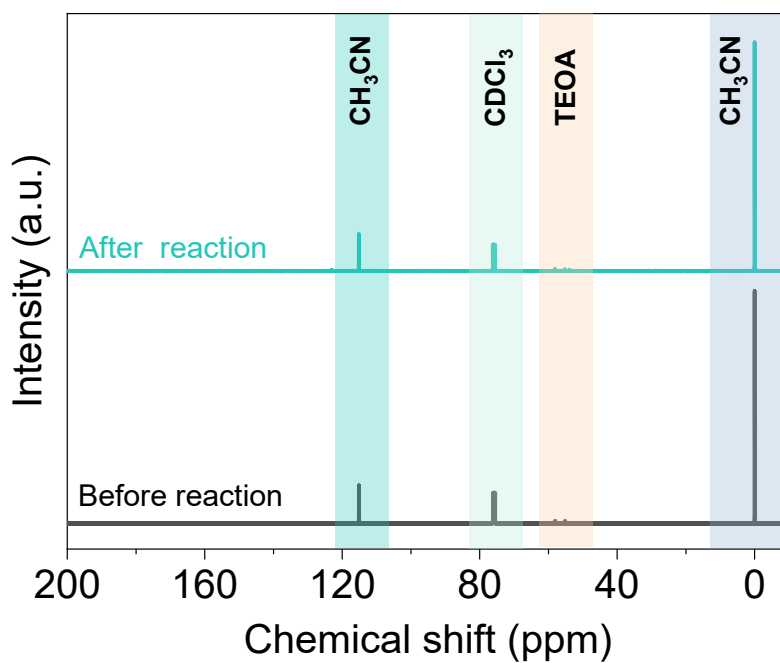


Figure S10. The liquid nuclear magnetic resonance (NMR) map before and after the reaction.

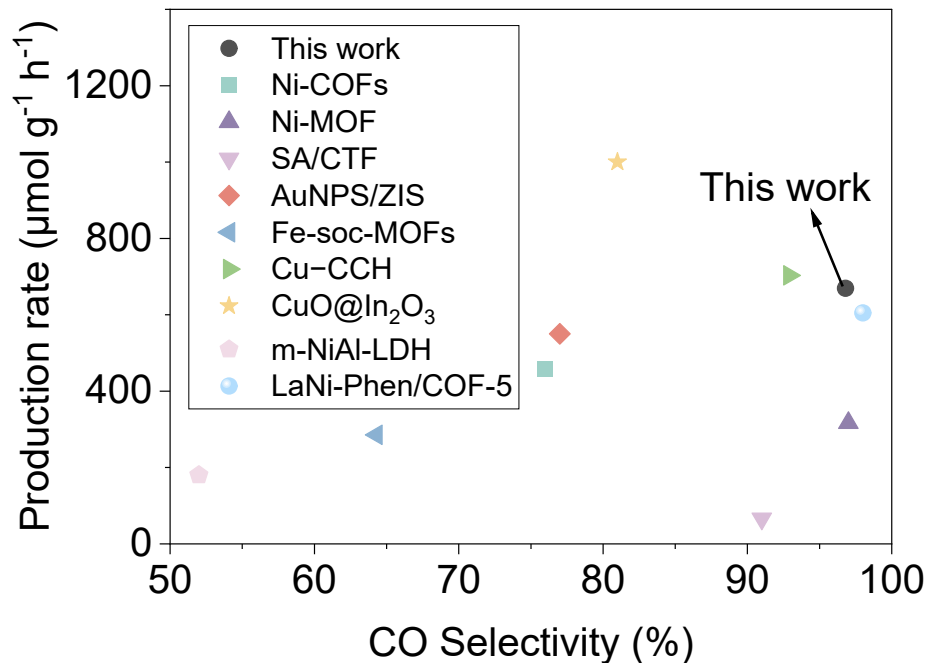


Figure S11. Comparison of the performances of La/Ni-MOF-3 in present work with some typical photocatalysts towards CO₂ reduction in similar reaction systems.

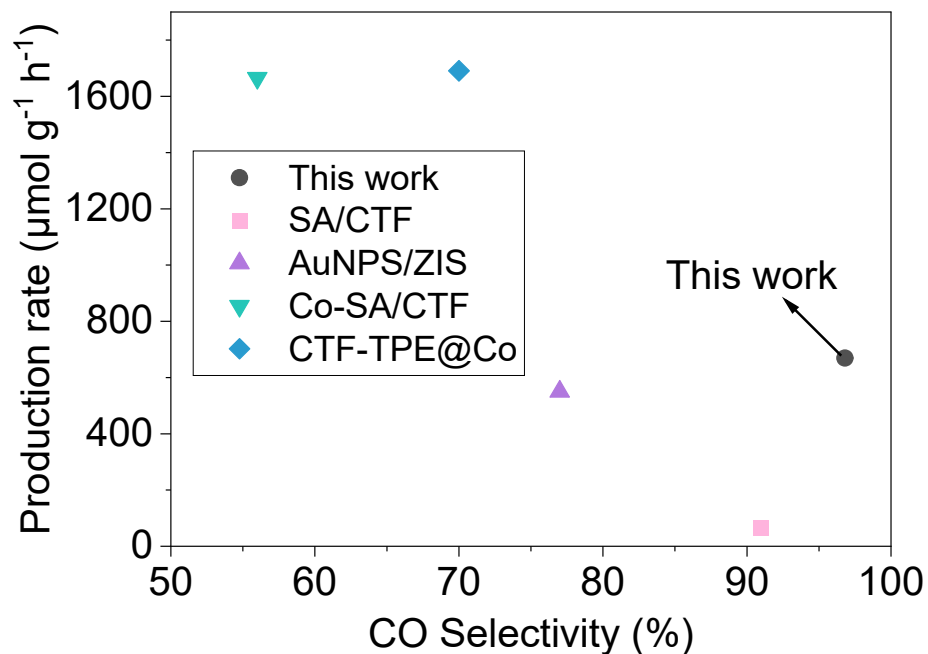


Figure S12. Comparison of the performances of La/Ni-MOF-3 in present work with some typical single-atom photocatalysts towards CO₂ reduction in similar reaction systems.

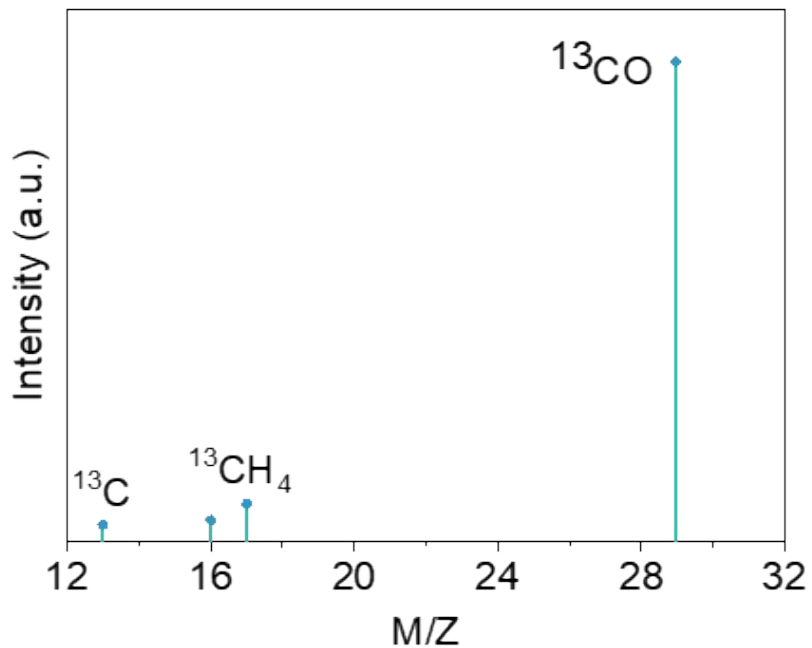


Figure S13. Mass spectra obtained for the photocatalytic reduction of $^{13}\text{CO}_2$ over La/Ni-MOF-3.

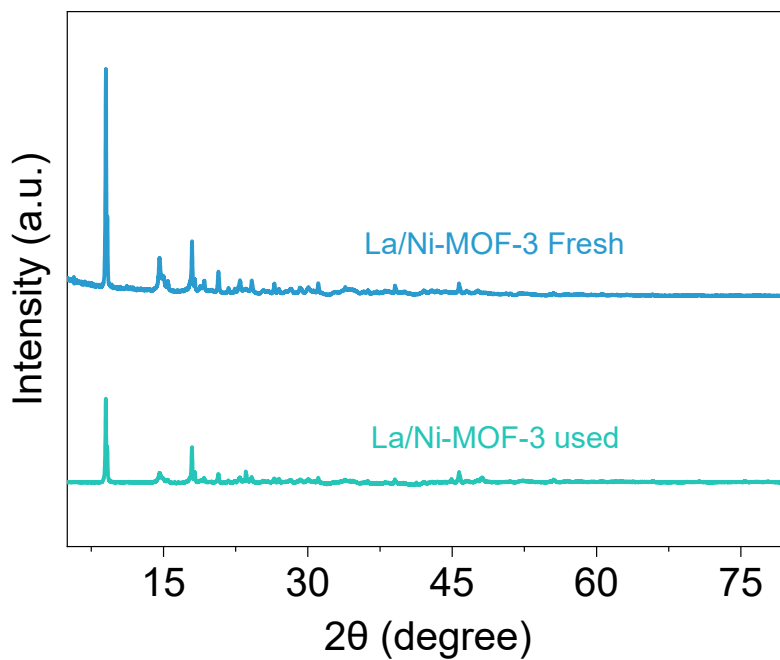


Figure S14. XRD patterns of the as-prepared La/Ni-MOF-3 photocatalyst before and after durability test.

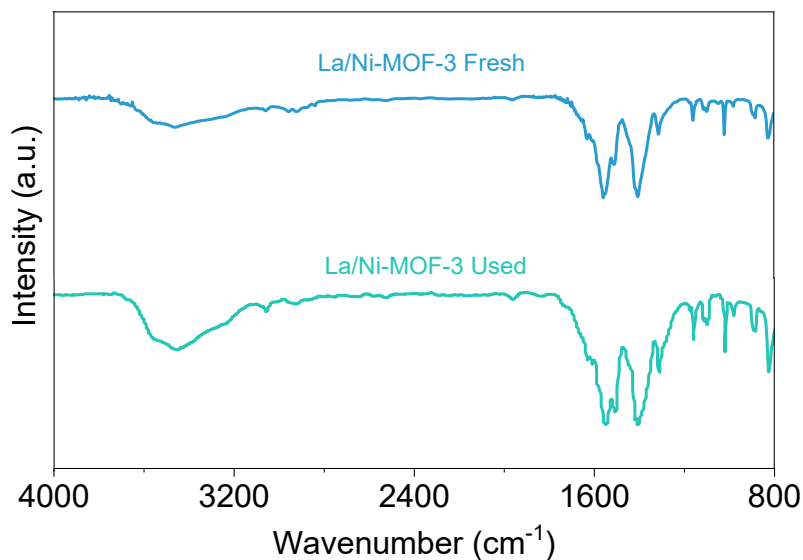


Figure S15. FTIR results of the as-prepared La/Ni-MOF-3 photocatalyst before and after durability test.

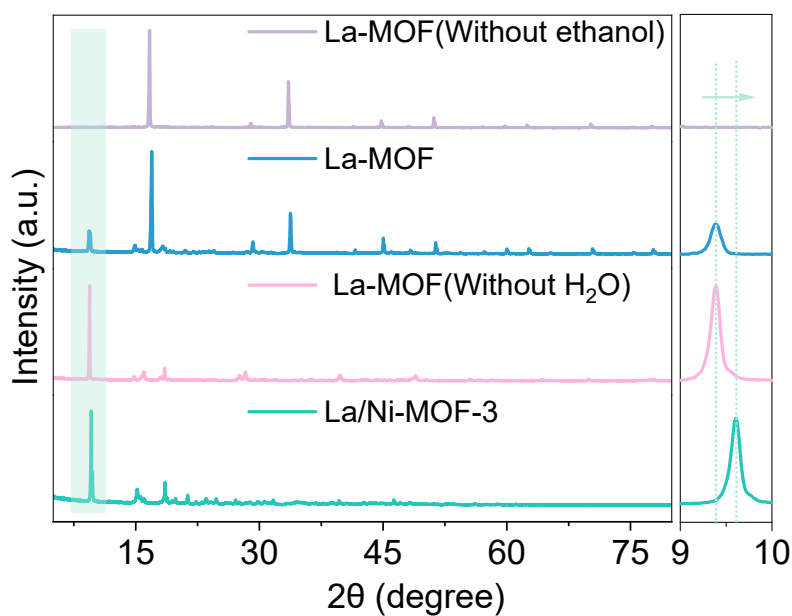


Figure S16. The XRD patterns of La/Ni-MOF-3 and La-MOF samples prepared by different reaction solvent compositions (more specifically, La-MOF is prepared in the solvent of DMF, H₂O and CH₃CH₂OH as described in the experimental section; the other two La-MOF samples are prepared by adjusting the solvent as indicated in the brackets).

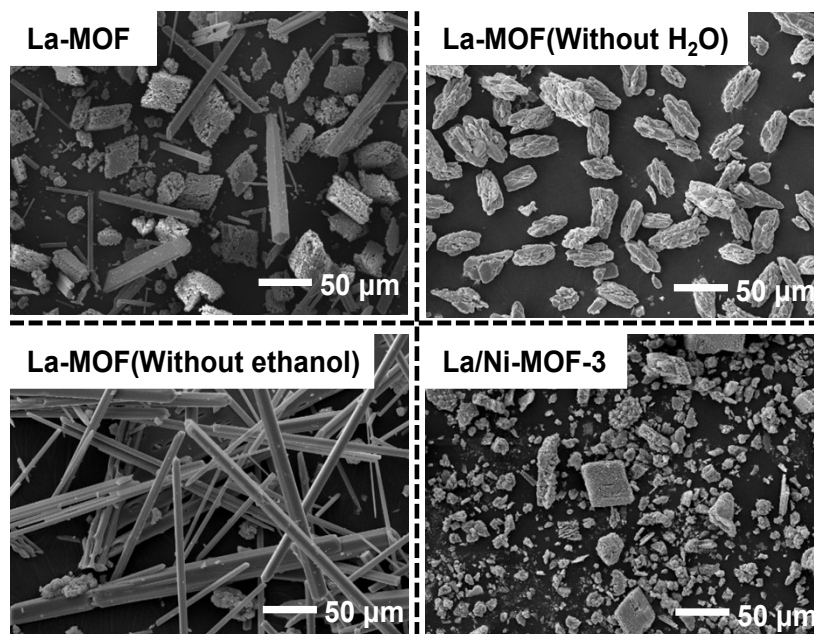


Figure S17. The SEM of La-MOF samples prepared by different reaction solvent compositions (more specifically, La-MOF is prepared in the solvent of DMF, H₂O and CH₃CH₂OH as described in the experimental section; the other two La-MOF samples are prepared by adjusting the solvent as indicated in the brackets) and La/Ni-MOF-3.

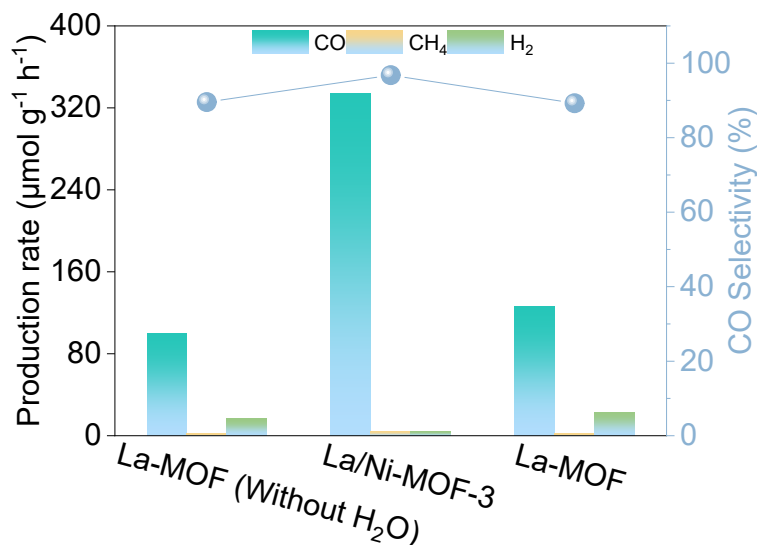


Figure S18. The photocatalytic activity of La/Ni-MOF-3 and La-MOF samples prepared by different reaction solvent compositions (more specifically, La-MOF is prepared in the solvent of DMF, H₂O and CH₃CH₂OH as described in the experimental section; La-MOF (Without H₂O) is prepared by adjusting the solvent as indicated in the bracket).

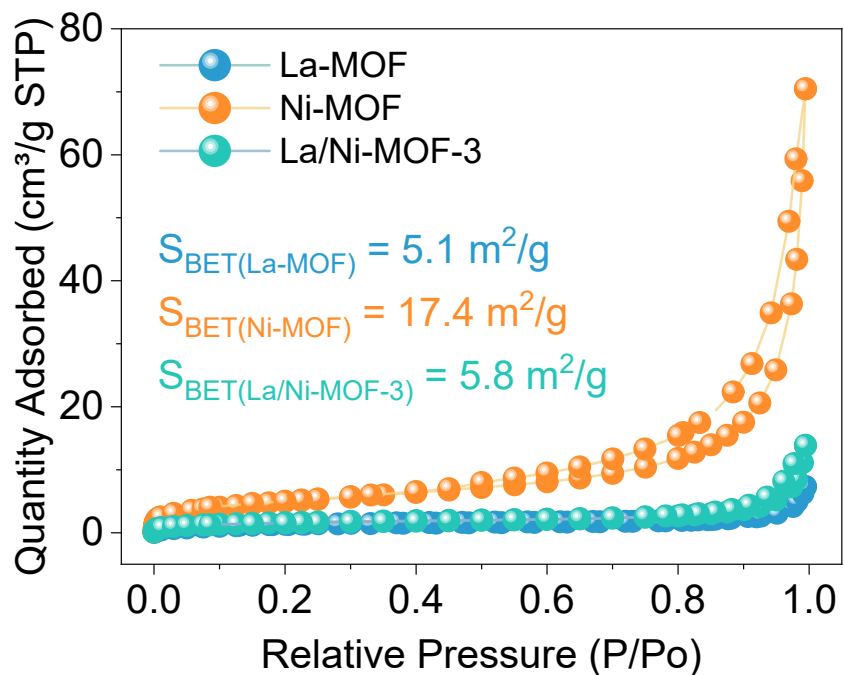


Figure S19. N_2 adsorption–desorption isotherms of La-MOF, Ni-MOF, and La/Ni-MOF-3.

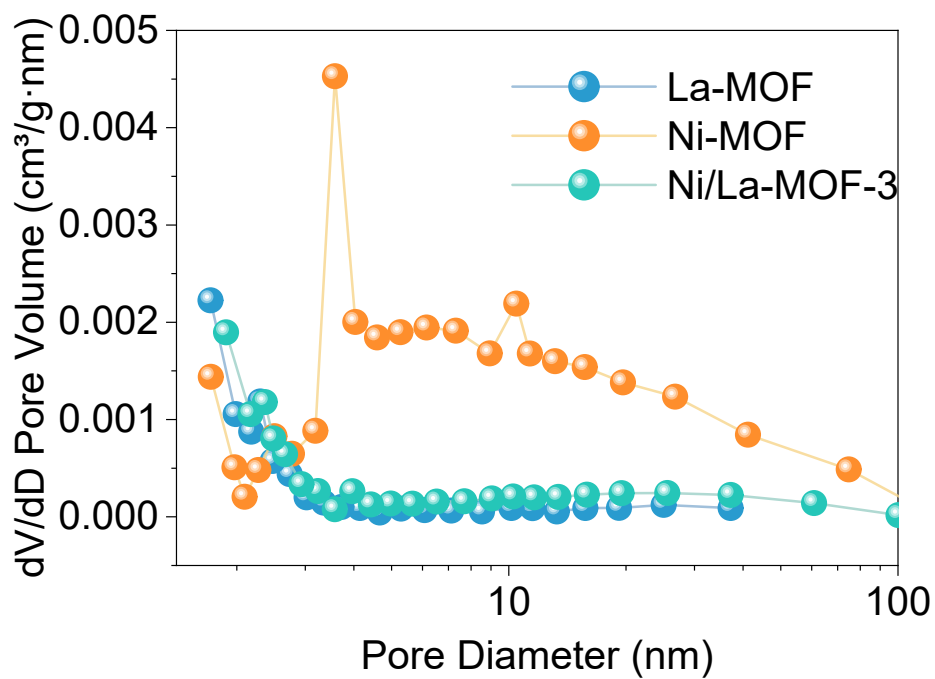


Figure S20. Pore diameter distribution of La-MOF, Ni-MOF, and La/Ni-MOF-3.

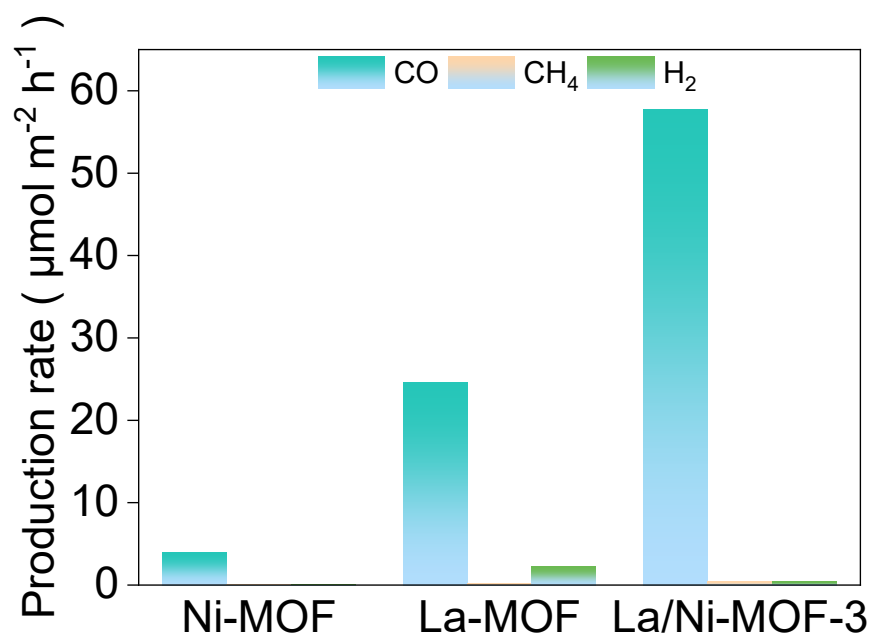


Figure S21. CO production rate in terms of BET specific surface area the as-prepared La-MOF, Ni-MOF, and La/Ni-MOF-3.

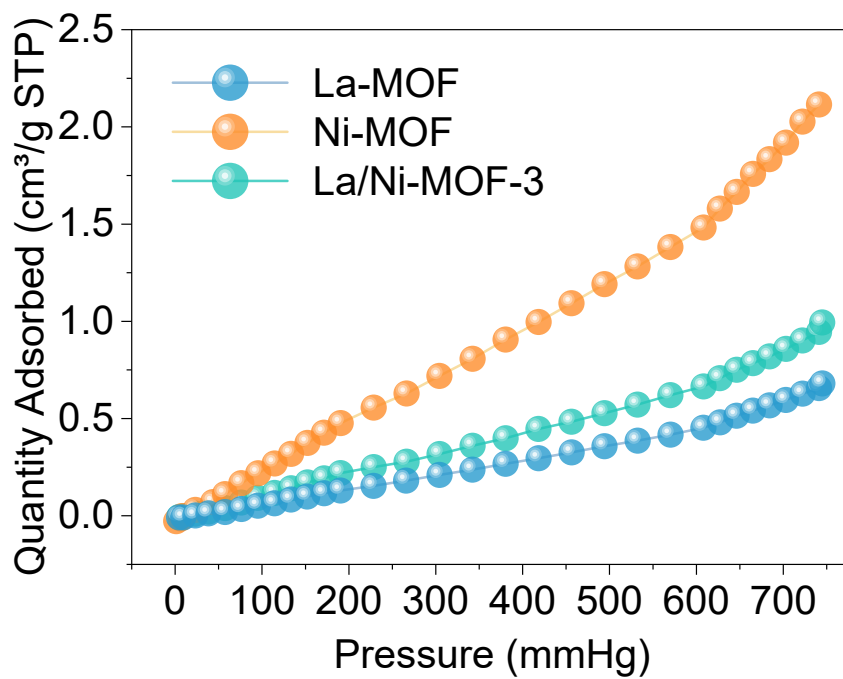


Figure S22. CO₂ adsorption isotherms of La-MOF, Ni-MOF, and La/Ni-MOF-3.

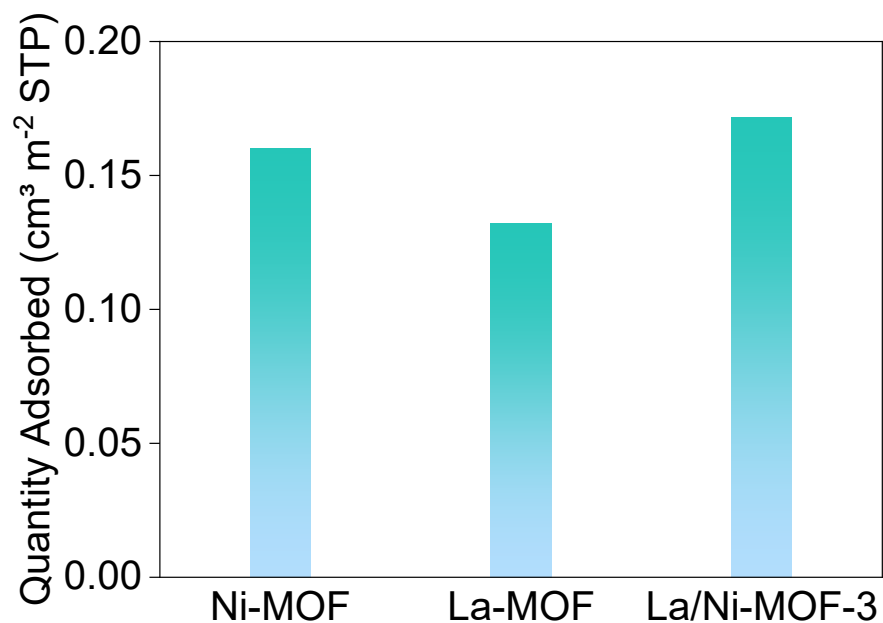


Figure S23. CO production rate in terms of BET specific surface area the as-prepared La-MOF, Ni-MOF, and La/Ni-MOF-3.

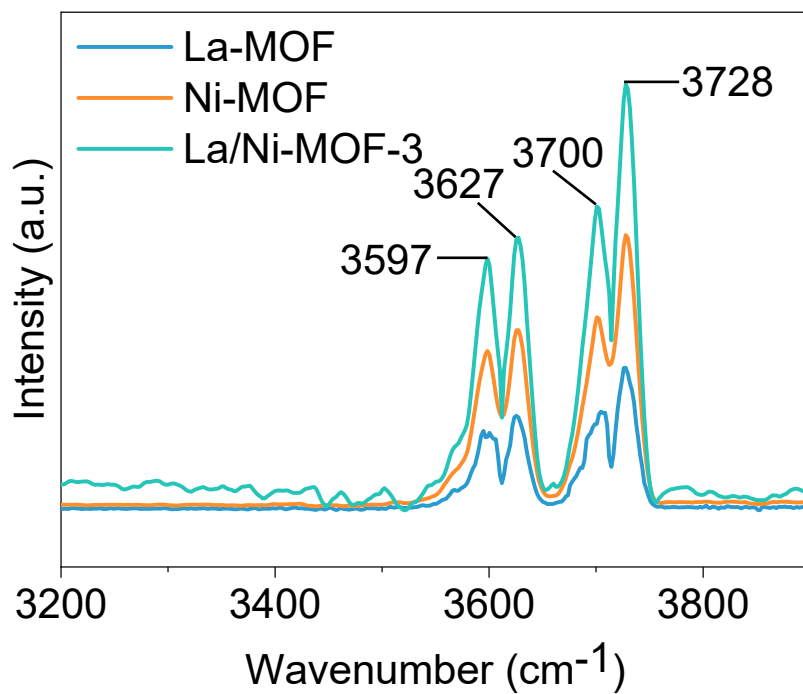


Figure S24. In situ DRIFTS spectra of CO₂ adsorption for La-MOF, Ni-MOF, and La/Ni-MOF-3.

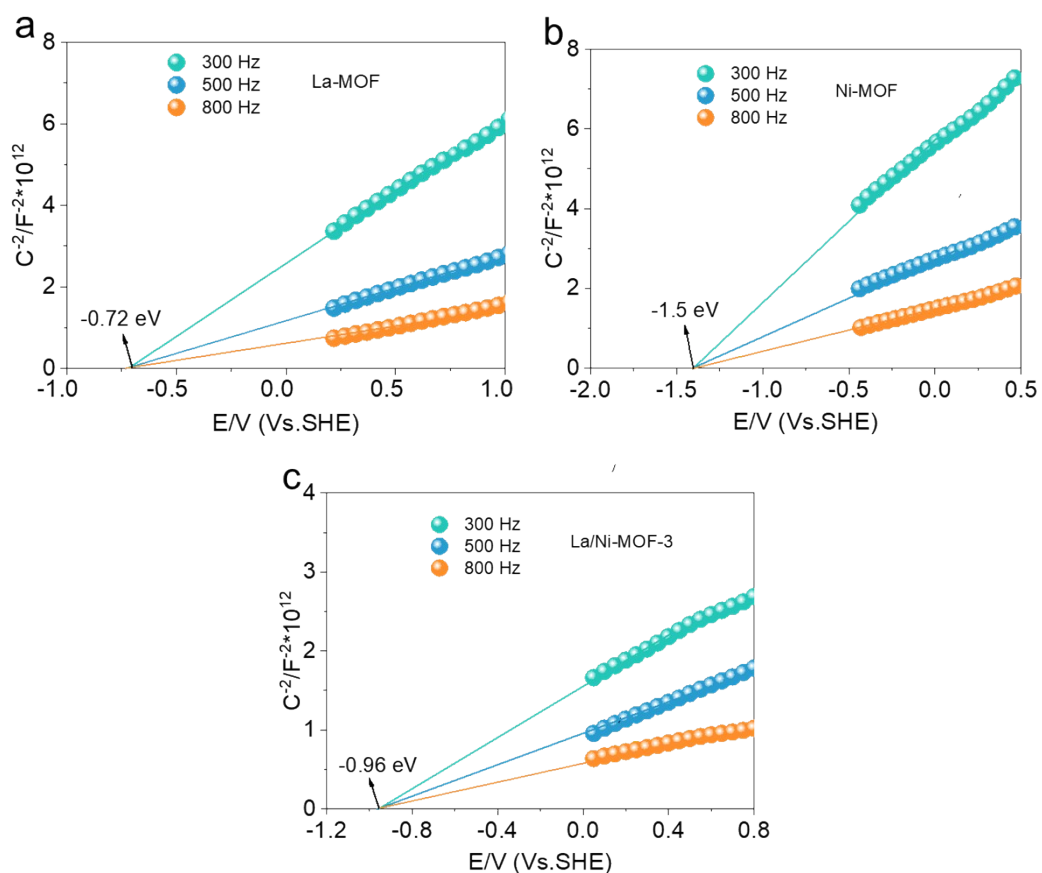


Figure S25. Mott-Schottky plots of (a) La-MOF, (b) Ni-MOF, and (c) La/Ni-MOF-3.

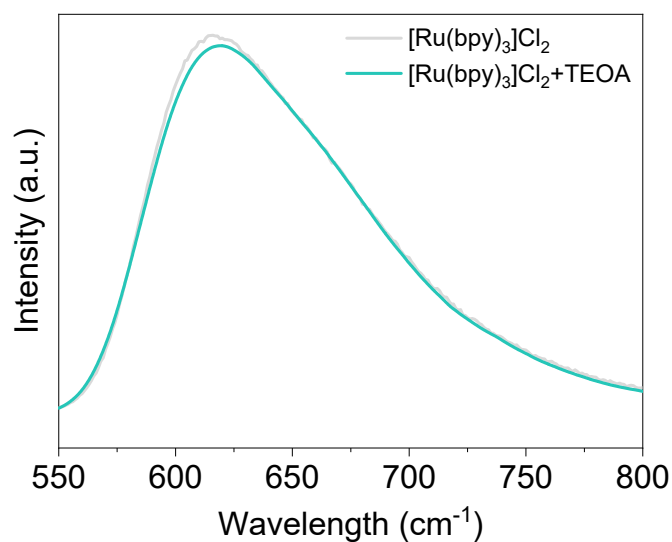


Figure S26. Steady state photoluminescence emission spectra of $[\text{Ru}(\text{bpy})_3]\text{Cl}_2$ (1 mg/mL) upon the addition of TEOA in a CO_2 degassed solution of $\text{CH}_3\text{CN}/\text{H}_2\text{O}$.

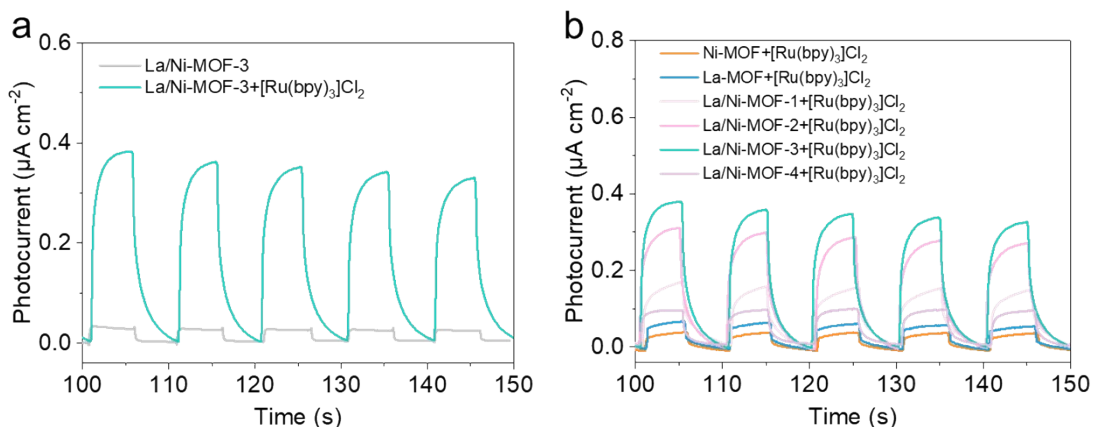


Figure S27. (a) Transient photocurrent response for La/Ni-MOF-3 and La/Ni-MOF-3 containing [Ru(bpy)₃]Cl₂. (b) Transient photocurrent response for La-MOF, Ni-MOF, and La/Ni-MOF-*X* in the case of containing [Ru(bpy)₃]Cl₂.

Table S1. ICP-MS results of La/Ni-MOF-*X* (*X*=1, 2, 3, and 4).

Samples	The molar ratio of La/Ni-MOF
La/Ni-MOF-1	La: Ni=109:1
La/Ni-MOF-2	La: Ni=48:1
La/Ni-MOF-3	La: Ni=32:1
La/Ni-MOF-4	La: Ni=12:1

Table S2. Comparison of the performances of La/Ni-MOF-3 in present work with some typical photocatalysts towards CO₂ reduction in similar reaction systems.

Catalyst	Light source	Photosensitizer/sacrificial agent	Irradiation time	Catalyst dosage	CO evolution rate $\mu\text{mol/g}$	Selectivity to CO	Refs.
La/Ni-MOF-3	$\lambda \geq 420$ nm 300W Xe	Ru(bpy) ₃ ²⁺ TEOA	2 h	3 mg	669.5	96.8%	this work
Co-MOF-NS	$\lambda \geq 420$ nm 300W Xe	Ru(bpy) ₃ ²⁺ TEOA	10 h	0.5 mg	27.1	70.1%	2
Cu-CCH	$\lambda \geq 420$ nm 300W Xe	Ru(bpy) ₃ ²⁺ TEOA	1 h	10 mg	703	92.9%	3
[DMC@Cu-CAT]-	$\lambda \geq 420$ nm 300W Xe	Ru(bpy) ₃ ²⁺	1 h	10 mg	133.36	---	4

PVK							
m-NiAl-LDH	300W Xe $\lambda \geq 600$ nm	Ru(bpy) ₃ ²⁺ TEOA	1 h	10 mg	90	52%	5
LaNi-Phen/COF-5	$\lambda \geq 420$ nm 300W Xe	Ru(bpy) ₃ ²⁺ BIH	1 h	10 mg	605.8	98.2%	6
CdSeTe/U iO-66	$\lambda \geq 420$ nm 300W Xe	Ru(bpy) ₃ ²⁺ TEOA	1 h	5 mg	228.68	---	7
Fe-soc-MOFs	$\lambda \geq 420$ nm 300W Xe	---	5 h	100 mg	285.6	64.3%	8
CuO@In ₂ O ₃	$\lambda \geq 420$ nm 300W Xe	Ru(bpy) ₃ ²⁺ TEOA	1 h	1 mg	500.86	81%	9
Ni-COFs	$\lambda \geq 420$ nm 300W Xe	Ru(bpy) ₃ ²⁺ TEOA	4 h	15 mg	915	76%	10
Ni-MOF	$\lambda \geq 420$ nm 300W Xe	Ru(bpy) ₃ ²⁺ TIPA	1 h	10 mg	317	97%	11
FeCoS ₂ - CoS ₂	$\lambda \geq 400$ nm 300W Xe	Ru(bpy) ₃ ²⁺ TEOA	1 h	0.5 mg	28.1	64%	12
ZnCo-OH QUNH	$\lambda \geq 420$ nm 300W Xe	Ru(bpy) ₃ ²⁺ TEOA	1 h	10 mg	134.2	76.9%	1
Cu- SA/CTF	$\lambda \geq 420$ nm 300W Xe	Ru(bpy) ₃ ²⁺ TEA	2 h	5 mg	66	91%	13
Au _{NPS} /ZIS	$\lambda \geq 420$ nm 300W Xe	Ru(bpy) ₃ ²⁺ TEOA	2 h	10 mg	550	77%	14
Co- SA/CTF	$\lambda \geq 420$ nm 300W Xe	Ru(bpy) ₃ ²⁺ TEOA	2 h	5 mg	1665	56%	15
CTF- TPE@Co	$\lambda \geq 420$ nm 300W Xe	Ru(bpy) ₃ ²⁺ TEOA	2 h	5 mg	1515	70%	16

References

1. F. Wang, R. Fang, X. Zhao, X.-P. Kong, T. Hou, K. Shen and Y. Li, Ultrathin Nanosheet Assembled Multishelled Superstructures for Photocatalytic CO₂ Reduction, *ACS Nano*, 2022, **16**, 4517-4527.
2. W. Chen, B. Han, C. Tian, X. Liu, S. Liang, H. Deng and Z. Lin, MOFs-derived ultrathin holey Co₃O₄ nanosheets for enhanced visible light CO₂ reduction, *Appl. Catal. B-environ*, 2019, **244**, 996-1003.
3. H. Liu, Y. Chen, H. Li, G. Wan, Y. Feng, W. Wang, C. Xiao, G. Zhang and Y. Xie, Construction of Asymmetrical Dual Jahn–Teller Sites for Photocatalytic CO₂ Reduction, *Angew. Chem. Int. Ed.*, 2023, **62**, e202304562.
4. K. Yuan, K. Tao, T. Song, Y. Zhang, T. Zhang, F. Wang, S. Duan, Z. Chen, L. Li, X. Zhang, D. Zhong, Z. Tang, T.-B. Lu and W. Hu, Large-Area Conductive MOF Ultrathin Film Controllably Integrating Dinuclear-Metal Sites and Photosensitizers to Boost Photocatalytic CO₂ Reduction with H₂O as an Electron Donor, *J. Am. Chem. Soc.*, 2024, **146**, 6893-6904.
5. L. Tan, S.-M. Xu, Z. Wang, Y. Xu, X. Wang, X. Hao, S. Bai, C. Ning, Y. Wang, W.

- Zhang, Y. K. Jo, S.-J. Hwang, X. Cao, X. Zheng, H. Yan, Y. Zhao, H. Duan and Y.-F. Song, Highly Selective Photoreduction of CO₂ with Suppressing H₂ Evolution over Monolayer Layered Double Hydroxide under Irradiation above 600 nm, *Angew. Chem. Int. Ed.*, 2019, **58**, 11860-11867.
6. M. Zhou, Z. Wang, A. Mei, Z. Yang, W. Chen, S. Ou, S. Wang, K. Chen, P. Reiss, K. Qi, J. Ma and Y. Liu, Photocatalytic CO₂ reduction using La-Ni bimetallic sites within a covalent organic framework, *Nat. Commun.*, 2023, **14**, 2473.
 7. L. Chen, Q. Tang, S. Wu, L. Zhang, L. Feng, Y. Wang, Y. Xie, Y. Li, J.-P. Zou and S.-L. Luo, Covalent coupling promoting charge transport of CdSeTe/UiO-66 for boosting photocatalytic CO₂ reduction, *Chin. Chem. Lett.*, 2023, **34**, 107903.
 8. X.-Y. Zhang, P. Wang, X.-Y. Lu, Y. Zhang and W.-Y. Sun, Synergistic effect on photocatalytic CO₂ reduction of facet-engineered Fe-soc-MOFs with photo-deposited PtO species, *Chem. Eng. J.*, 2023, **476**, 146560.
 9. X. Liu, Y. Wu, Y. Li, X. Yang, Q. Ma and J. Luo, MOF-on-MOF-derived CuO@In₂O₃ s-scheme heterojunction with core-shell structure for efficient photocatalytic CO₂ reduction, *Chem. Eng. J.*, 2024, **485**, 149855.
 10. W. Zhong, R. Sa, L. Li, Y. He, L. Li, J. Bi, Z. Zhuang, Y. Yu and Z. Zou, A Covalent Organic Framework Bearing Single Ni Sites as a Synergistic Photocatalyst for Selective Photoreduction of CO₂ to CO, *J. Am. Chem. Soc.*, 2019, **141**, 7615-7621.
 11. X.-K. Wang, J. Liu, L. Zhang, L.-Z. Dong, S.-L. Li, Y.-H. Kan, D.-S. Li and Y.-Q. Lan, Monometallic Catalytic Models Hosted in Stable Metal–Organic Frameworks for Tunable CO₂ Photoreduction, *ACS Catal.*, 2019, **9**, 1726-1732.
 12. Y. Wang, S. Wang, S. L. Zhang and X. W. Lou, Formation of Hierarchical FeCoS₂–CoS₂ Double-Shelled Nanotubes with Enhanced Performance for Photocatalytic Reduction of CO₂, *Angew. Chem. Int. Ed.*, 2020, **59**, 11918-11922.
 13. G. Huang, Q. Niu, Y. He, J. Tian, M. Gao, C. Li, N. An, J. Bi and J. Zhang, Spatial confinement of copper single atoms into covalent triazine-based frameworks for highly efficient and selective photocatalytic CO₂ reduction, *Nano Res.*, 2022, **15**, 8001-8009.
 14. S. Si, H. Shou, Y. Mao, X. Bao, G. Zhai, K. Song, Z. Wang, P. Wang, Y. Liu, Z. Zheng, Y. Dai, L. Song, B. Huang and H. Cheng, Low-Coordination Single Au Atoms on Ultrathin ZnIn₂S₄ Nanosheets for Selective Photocatalytic CO₂ Reduction towards CH₄, *Angew. Chem. Int. Ed.*, 2022, **61**, e202209446.
 15. G. Huang, G. Lin, Q. Niu, J. Bi and L. Wu, Covalent triazine-based frameworks confining cobalt single atoms for photocatalytic CO₂ reduction and hydrogen production, *J. Mater. Sci. Technol.*, 2022, **116**, 41-49.
 16. A. Jana, A. Maity, A. Sarkar, B. Show, P. A. Bhoje and A. Bhunia, Single-site cobalt catalyst embedded in a covalent triazine-based framework (CTF) for photocatalytic CO₂ reduction, *J. Mater. Chem. A*, 2024, **12**, 5244-5253.